arXiv:1603.04457v1 [cond-mat.mtrl-sci] 14 Mar 2016

All-Optical Materials Design of Chiral Edge Modes in Transition-Metal Dichalcogenides

Martin Claassen,[1,2*] Chunjing Jia[2], Brian Moritz[2], Thomas P. Devereaux[2]

[1]Department of Applied Physics, Stanford University, CA 94305, USA
[2]Stanford Institute for Materials and Energy Sciences, SLAC & Stanford University, CA 94025, USA

*To whom correspondence should be addressed; E-mail: mclaassen@stanford.edu.

Manipulating materials properties far from equilibrium recently garnered significant attention, with experimental emphasis on transient melting, enhancement, or induction of electronic order [1, 2, 3, 4]. A more tantalizing aspect of the matter-light interaction regards the possibility to access dynamical steady states with distinct non-equilibrium phase transitions to affect electronic transport [5, 6, 7, 8, 9]. Here, we show that the interplay of crystal symmetry and optical pumping of monolayer transition-metal dichalcogenides (TMDCs) provides a novel avenue to engineer topologically-protected chiral edge modes. In stark contrast to graphene [10, 11] and previously-discussed toy models [8, 13, 14], the underlying generic mechanism relies on the intrinsic three-band nature of TMDCs near the band edges. Photo-induced band inversions scale linearly in applied pump field and exhibit a transition from one to two chiral edge modes upon sweeping from red to blue detuning. We develop a strategy to understand non-equilibrium Floquet-Bloch bands and topological transitions directly from *ab initio* calculations, and illustrate for

the example of WS$_2$ that control of chiral edge modes can be dictated solely from symmetry principles and is not qualitatively sensitive to microscopic materials details.

Viewed naïvely as semiconducting analogs of graphene, trigonal-prismatic monolayers of MoS$_2$, MoSe$_2$, WS$_2$ and WSe$_2$ possess sizeable intrinsic band gaps due to broken inversion symmetry [13], that can be expected to sustain intense sub-gap pump pulses while limiting absorption. Prior theoretical studies established that the band edges at **K** and **K**$'$ are dominated by transition-metal d-orbitals, which split into three groups with irreducible representations (IRs) $A'\{d_{3z^2-r^2}\}$, $E', \bar{E}'\{d_{x^2-y^2} \pm id_{2xy}\}$ and $E'', \bar{E}''\{d_{xz} \pm id_{yz}\}$ of the C_{3h} point group [15, 16]. Generalizing graphene, these valleys are well-captured in equilibrium by a degenerate Kramers' pair of massive Dirac fermions, giving rise to valley-Hall [13] and spin-Hall [17, 18] effects.

Out of equilibrium, dynamical breaking of time-reversal symmetry was demonstrated to lift the valley degeneracy for WS$_2$ and WSe$_2$ via off-resonant optical pumping with circularly-polarized light [8, 9]. In this case, the selection rules for a massive Dirac fermion entail that the handedness of pump polarization selectively addresses either the **K** or **K**$'$ valley, imparting an AC Stark shift on only one of the valleys. Analogously, the photo-excitation can selectively populate valleys, enabling spin and valley valley currents using circular or linear polarization [19, 20, 21].

Conceptually simple, irradiation with a sufficiently broad pump pulse dresses the original electronic bands by multiples of the photon frequency, with electric dipole coupling resulting in an effective steady-state band structure; Floquet-Bloch theory then corresponds precisely to the classical limit of strong pump fields that are indistinguishable before and after photon absorption or emission. One paradigmatic model of such "Floquet-Bloch bands" is graphene [10, 11, 12], where circularly-polarized light can break time-reversal

symmetry to dynamically lift the Dirac point degeneracies. While Floquet-Bloch states were indeed observed recently via micro-wave pumping Dirac cones on the surface of topological insulators [6, 7], an extension to proper topological phase transitions is still well beyond experimental reach due to the tremendous required intensity A to open a sizeable gap $\Delta \sim A^2/\Omega$ [10] for above-bandwidth pump frequencies.

Even more tantalizingly, it was predicted that effective TMDC toy models of "graphene with a gap" admit in theory an optically-induced *quantum* Hall effect with a single chiral mode localized at the sample edge. A high-frequency pump $\Omega \to \infty$ well above the bandwidth can in principle close and invert the equilibrium band gap at a single valley [14], however requiring tremendous pump intensities as the relative gap shift scales as $\sim ev_D A^2/\Omega^3$ with v_D the Dirac velocity. Alternatively, it was proposed that a resonant pump beam can hybridize the massive Dirac fermion valence and conduction bands and thereby generate a single chiral edge mode [8] at lower pump strength. However, we show instead that such a simple description of TMDCs fails to hold for optical pumping; here, the added complexity of a microscopic materials description opens up a novel avenue to photo-induce chiral edge modes in a realistic experimental setting.

Central to this paper, dipole transitions to higher-lying bands as determined directly from *ab initio* calculations and underlying symmetry considerations are crucial for a description of photo-induced topological band inversions in TMDCs. To understand the breakdown of "graphene with a gap", consider a monolayer ribbon irradiated by circularly-polarized light, for collinear sample and polarization planes [Fig. 1(a)]. In graphene, the low-energy E'' bands are separated from A'' bands by more than 10eV at $\mathbf{K}, \mathbf{K}'$ [22], hence optical frequencies can be treated safely within the canonical low-energy Dirac model of $\boldsymbol{\pi}$ orbitals. In contrast, the band structures of prototypical TMDC monolayers [Fig. 1(b)] possess a E' band only $\sim$ 2eV above the conduction band (CB) [Fig. 1(b)], and E''

bands in the same vicinity [23, 24, 25, 26]. Circularly-polarized light at close-to-bandgap pump frequencies therefore couples the A' CB to *both* the E' valence band (CB) and the $\bar{E}'$ higher-energy conduction band (XB), while leaving the E'' bands decoupled in the absence of multipole transitions.

Consider first slightly red-detuned pumping below the band edge [Fig. 2(a)]. Here, a ring of states from the higher-energy XB is brought into resonance with the CB, while simultaneously limiting absorption and heating by avoiding resonant coupling between the VB and CB. At the band edge, C_{3h} dipole selection rules [Fig. 2(e)] dictate that absorption of a photon couples transitions $A' \to \bar{E}' \to E' \to A'$. At $\mathbf{K}'$, the bare CB $|m = 0; A', CB\rangle$ couples to the XB dressed by a single emitted photon $|m = -1; E', XB\rangle$ as well as the VB dressed by a single absorbed photon $|m = +1; \bar{E}', VB\rangle$. Both transitions, though off-resonant, are energetically favorable, leading to a significant Stark shift at $\mathbf{K}'$ [Fig. 2(b)]. Conversely, at $\mathbf{K}$ the IRs of VB and XB are reversed. Here, the conduction band couples to the VB dressed by a single emitted photon $|m = -1; E', VB\rangle$ as well as the XB dressed by a single absorbed photon $|m = +1; \bar{E}', XB\rangle$. Both transitions are energetically unfavorable, leading to a negligible shift of the band edge. Slightly away from $\mathbf{K}$ and $\mathbf{K}'$, electric dipole coupling lifts the ring of degeneracy between the CB and XB and opens a photo-induced hybridization gap at both valleys [Fig. 2(b)], which scales *linearly* with weak pump fields. Crucially, the resulting Floquet-Bloch bands exhibit a topological 'band inversion' with the orbital character flipped close to the valley minimum at *both valleys* [Fig. 2(b)].

To discern whether the band inversions can be non-trivial, we devise effective Floquet "low-energy" models of the hybridization gaps. We start from the generic description $\hat{H}_0 = \hat{\mathbf{p}}^2/2m_0 + V(\mathbf{r})$ of a semiconductor in the absence of spin-orbit coupling and excitonic effects, where $V(\mathbf{r})$ is the crystal potential. In equilibrium, starting from an *ab*

initio Bloch eigenbasis at a single high-symmetry point, the dispersion and orbital content follow from canonical **k**.**p** theory by perturbing in momentum deviation **k** under replacement $\hat{\mathbf{p}} \rightarrow \hat{\mathbf{p}} + \hbar\mathbf{k}$ [27]. In the presence of a time-periodic field $\mathbf{A}(t)$, a straightforward generalization uses a *Floquet eigenbasis* of the generic non-equilibrium problem $\hat{H}_0(t) = \frac{1}{2m_0}\left[\hat{\mathbf{p}} + e\mathbf{A}(t)\right]^2 + V(\mathbf{r})$. This basis can be obtained from density-functional theory calculations via knowledge of the equilibrium band energies and dipole transition matrix elements. Note that this Floquet **k**.**p** theory is non-perturbative in the applied pump field and naturally accounts for multi-photon coupling to higher-energy CBs, XBs and deeper VBs, as well as local inter-orbital dipole transitions. An effective low-energy description of the photo-induced gaps can now be devised in Floquet basis in analogy to the equilibrium problem, by considering a perturbation in crystal momentum $\hat{\mathbf{p}} \rightarrow \hat{\mathbf{p}} + \hbar\mathbf{k}$ and downfolding onto effective two-band Floquet models using canonical Löwdin perturbation theory.

Central to the robustness of this proposal, the form of these effective models is determined solely from symmetry and is universal to trigonal-prismatic TMDC monolayers. To see this, first consider **K**: Here, the Floquet eigenbasis [Fig. 2(b)] $|\Psi_1\rangle$ ($|\Psi_2\rangle$) admixes $|m = 0; A', CB\rangle$ with $|m = -1; E', VB\rangle$, $|m = +1; \bar{E}', XB\rangle$ ($|m = -1; \bar{E}', XB\rangle$ with $|m = -2; A', CB\rangle$, $|m = 0; E', VB\rangle$), linear in field A_0. Constrained by crystal symmetry, we find that the effective Floquet physics at **K** is generically determined by a *p-d* Dirac model [Supplementary Material]:

$$\hat{H}_\mathbf{K}(\mathbf{k}) = \epsilon_0(\mathbf{k}) + \begin{bmatrix} \frac{M}{2} - B|\mathbf{k}|^2 & v_p k_- - v_d k_+^2 \\ v_p k_+ - v_d k_-^2 & -\frac{M}{2} + B|\mathbf{k}|^2 \end{bmatrix} \tag{1}$$

Here, v_p, v_d are linear functions in field strength, and an additional purely dispersive term $\epsilon_0(\mathbf{k}) = \Delta_0 + \Delta_2|\mathbf{k}|^2$ breaks particle-hole symmetry. While the parameters depend on the details of the Bloch states near the Dirac points, overall topological considerations can be

gleaned simply from Eq. 1. In the absence of v_d, Eq. (1) describes a conventional massive Dirac fermion, with M (B) the Dirac (inverse band) mass, and v_p the Dirac velocity. The orbital character exhibits a p-wave winding around $\mathbf{K}$ and mirrors the quantum anomalous Hall effect in $\text{Hg}_y\text{Mn}_{1-y}\text{Te}$ quantum wells [29]. Switching on v_d imparts a trigonal distortion by reducing the continuous rotational symmetry around $\mathbf{K}$ to C_3, and introduces instead a 'd-wave' winding in the limit of $\sqrt{B/M}\, v_d \gg v_p$.

At $\mathbf{K}'$ interchanged IRs $E', \bar{E}'$ entail a strongly-admixed Floquet eigenbasis as well as a significant Stark shift. However selection rules forbid a coupling between $|\Psi_1\rangle, |\Psi_2\rangle$ linear in $\mathbf{k}$ – instead, one finds that the two bands couple to quadratic order in $\sim A_0 k_+ k_-$, via intermediate states $m = 0; E'$ XB or $m = -1; A'$ CB. The effective Hamiltonian for $\mathbf{K}'$ in this case generically reads

$$\hat{H}_{\mathbf{K}'}(\mathbf{k}) = \epsilon_0'(\mathbf{k}) + \begin{bmatrix} \frac{M'}{2} - B'|\mathbf{k}|^2 & v'|\mathbf{k}|^2 \\ v'|\mathbf{k}|^2 & -\frac{M'}{2} + B'|\mathbf{k}|^2 \end{bmatrix} \tag{2}$$

with v' a rotationally-symmetric band mixing term.

At $\mathbf{K}$ $(\mathbf{K}')$, the band ordering is inverted when $M/B > 0$ $(M'/B' > 0)$. If the orbital character of Floquet-Bloch bands in the remaining Brillouin zone is sufficiently benign, we can draw conclusions on the global topology by understanding separately the band inversions at $\mathbf{K}$ and $\mathbf{K}'$. Rewriting Eqs. (1), (2) in terms of Pauli matrices $\hat{H} = \epsilon_0(\mathbf{k}) + \boldsymbol{\sigma} \cdot \mathbf{d}(\mathbf{k})$, the local Berry curvature follows from the winding $\mathcal{F}(\mathbf{k}) = \frac{1}{2}\hat{\mathbf{d}}(\mathbf{k}) \cdot (\partial_{k_x}\hat{\mathbf{d}}(\mathbf{k}) \times \partial_{k_y}\hat{\mathbf{d}}(\mathbf{k}))$ with $\hat{\mathbf{d}}(\mathbf{k}) = \mathbf{d}(\mathbf{k})/|\mathbf{d}(\mathbf{k})|$. One can see by inspection that the absence of $\hat{\boldsymbol{\sigma}}_y$ in Eq. (2) enforces $\mathcal{F}(\mathbf{k}) = 0$; therefore, the photo-induced band inversion around $\mathbf{K}'$ is necessarily trivial. Conversely, the band inversion at $\mathbf{K}$ is topological and triggers a change in the Chern number $\mathcal{C}$, which can be evaluated via appropriate compactification of $\mathbf{k}$-space $\mathbb{R}^2$ to a non-contractible manifold [Supplementary Material].

Consider first the limit of a massive Dirac model with $v_d = 0$. In this case, the Chern

6

number changes from $\mathcal{C} = 0$ for $B/M < 0$ to $\mathcal{C} = \pm 1$ for $B/M > 0$, inducing a single chiral edge mode at the sample boundary that spans the photo-induced hybridization gap. Then, switching on v_d introduces a trigonal distortion of the Floquet-Bloch bands around $\mathbf{K}$ up to a critical strength $v_d^2 = B/Mv_p^2$, at which the Floquet-Bloch bands close the gap at *three points* away from $\mathbf{K}$, related by C_3. Correspondingly, this topological transition changes $\mathcal{C}$ by 3, to $\mathcal{C} = \mp 2$, entailing not one but *two chiral edge modes* at the sample boundary.

While the relevant Floquet basis is predominantly built from only the $m = 0$ CB and $m = -1$ XB for a red-detuned pump, the p-wave coupling v_p between the two is necessarily mediated via the VB, highlighting the necessity of a minimal three-band description. The d-wave term v_d instead results from direct coupling between CB and XB.Strong optical absorption in TMDC monolayers indicates a large dipole transition matrix element between VB and CB, suggesting that a red-detuned pump will generically reach only the $C = 1$ phase.

Conversely, consider the opposite regime of a sufficiently blue-detuned pump [Fig. 2(c)]. Here, a ring of VB states is brought into resonance with the CB near $\mathbf{K}, \mathbf{K}'$ while pushing the photon-dressed XB into the equilibrium band gap. Electric dipole coupling again opens photo-induced hybridization gaps, both at the bottom of the CB and top of the VB [Fig. 2(d)], and the symmetry analysis mirrors the discussion of the red-detuned case above, leading to equivalent effective Hamiltonians at $\mathbf{K}, \mathbf{K}'$ (1), (2). However, linear in $\mathbf{k}$ coupling between the $m = 0$ CB and the $m = +1$ VB is now necessarily mediated via the XB (or other $\bar{E}'$ bands separated further in energy), whereas the d-wave term v_d follows directly from dipole coupling between VB and CB and thus dominates over v_p. One can thus generically expect a frequency-tunable Floquet Chern insulator in monolayer TMDCs, upon tuning the pump from red to blue detuning.

7

To illustrate the above predictions, we now consider WS_2 as a prototypical TMDC monolayer. First, we perform *ab initio* DFT calculations to derive an effective minimal tight-binding model of three $A', E', \bar{E}'$ Wannier orbitals localized on the transition metal [Fig. 1(b,c)]. The resulting Floquet spectrum on a ribbon is depicted in Fig. 3. In equilibrium [Fig. 3(a)], WS_2 already hosts a pair of trivial edge states in analogy to zigzag edges of graphene, with right (left) propagating modes at the **K** (**K**$'$) point that span the band gap. A weak, red-detuned pump field opens a hybridization gap at the bottom of the CB, spanned by a *single* chiral mode at **K** [Fig. 3(b)], localized at the sample edge. The photo-induced gap scales linearly with weak A, but closes and reopens at a critical pump strength, transitioning again to a trivial phase without chiral modes. Conversely, for a blue-detuned pump [Fig. 3(c)] a *second* chiral edge mode appears, spanning the hybridization gaps both at the bottom of the CB and the top of the VB.

The appearances of edge modes in ribbon spectra are in excellent agreement with effective model parameters [Eqs. (1), (2)] derived from the Wannier tight-binding description. Fig. 4(c) depicts M/B and the ratio of $p-/d-$wave couplings that determine the Chern number [Fig. 4(b)], in perfect correspondence with a rigorous calculation of the Floquet Chern number [28] in the Wannier tight-binding model [Fig. 4(d), see supplement]. For weak fields, deep within both the red- and blue-detuned regimes, the sign of the Dirac M and band B mass are equal in the topologically-nontrivial phase. Increasing A closes and reopens the Floquet gap at **K**, flips the sign of M and uninverts the bands to reach a trivial phase with $C = 0$. When $C \neq 0$, the Chern number follows from trigonal distortion and changes from $C = 1$ for red detuning to $C = 2$ for blue detuning.

Having checked the validity of Floquet **k.p** theory in the tight-binding model, we now turn to the full *ab initio* problem: To quantify the effects of multi-photon resonances, as well as local inter-orbital dipole transitions not captured in a tight-binding model, we

8

consider an *ab initio* 185-band description of band energies and dipole transition matrix elements at $\mathbf{K}$ and $\mathbf{K'}$ and calculate the model parameters of eqns. (2), (1), taking into account up to four-photon processes. The bands closest to the equilibrium gap are depicted in Fig. 4(e). The resulting $\mathbf{k.p}$ classification is depicted in Fig. 4(f). Crucially, while the resonance lines distort due to effects not accounted for in the tight-binding model, the frequency-dependent switch from $C = 1$ to $C = 2$ as well as the reclosing of the hybridization gap and transition back to a trivial regime for increasing pump strength remains qualitatively the same. This suggests that the mechanism of photo-induced chiral edge modes described in this work is largely robust at weak fields to the microscopic details of the material.

The guiding theme of this work has been to build a bridge between the rapidly developing field of monolayer transition-metal dichalcogenides and topological phase transitions out of equilibrium, to provide a route towards achieving the latter in an experimentally-attainable setting. We have shown that the three-band nature of the valleys in prototypical WS_2 leads to a new mechanism to 'switch' on or off one or two chiral edges with near band-gap optical irradiation. The resulting photo-induced gap in the single-particle spectrum scales linearly with pump strength, suggesting substantial energy scales already at low fields, while simultaneously ensuring minimal heating with sufficient detuning from the band edge. Our theoretical analysis of the out-of-equilibrium valley band inversions connects directly with equilibrium *ab initio* calculations, whereas the ensuing topology of Floquet-Bloch bands relies purely on generic symmetry arguments, suggesting that the predictions are robust to microscopic detail and should be observable in a range of monolayer TMDC materials. Finally, our first-principles and theoretical analysis provides a promising strategy to predict and design topological states out of equilibrium in other semiconductor materials.

References and Notes

[1] Schmitt, F. *et al.* Transient electronic structure and melting of a charge density wave in TbTe$_3$. *Science* 321, 1649–1652 (2008).

[2] Fausti, D. *et al.* Light-induced superconductivity in a stripe-ordered cuprate. *Science* 331, 189–191 (2011).

[3] Kim, K.W. *et al.* Ultrafast transient generation of spin-density-wave order in the normal state of BaFe$_2$As$_2$ driven by coherent lattice vibrations. *Nature Mater.* 11, 497–501 (2012).

[4] Mankowsky, R. *et al.* Nonlinear lattice dynamics as a basis for enhanced superconductivity in YBa$_2$Cu$_3$O$_{6.5}$. *Nature* 516, 71–73 (2014).

[5] Lindner, N.H., Refael, G. & Galitski, V. Floquet topological insulator in semiconductor quantum wells. *Nature Phys.*, 7, 490–495 (2011).

[6] Wang, Y.H., Steinberg, H. Jarillo-Herrero, P. & Gedik, N. Observation of floquet-bloch states on the surface of a topological insulator. *Science* 342, 453–457 (2013).

[7] Mahmood, F. *et al.* Selective scattering between FloquetBloch and Volkov states in a topological insulator *Nature Phys.* adv. online pub. Jan. 2016.

[8] Sie, E.J. *et al.* Valley-selective optical stark effect in monolayer ws2. *Nature Mat.* 14, 290–294 (2014).

[9] Kim, J. *et al.* Ultrafast generation of pseudo-magnetic field for valley excitons in wse2 monolayers. *Science* 346, 1205–1208 (2014).

[10] Oka, T. & Aoki, H. Photovoltaic hall effect in graphene. *Phys. Rev. B* 79, 081406 (2009).

[11] Kitagawa, T., Oka, T., Brataas, A., Fu, L. & Demler, E. Transport properties of nonequilibrium systems under the application of light: Photoinduced quantum hall insulators without landau levels. *Phys. Rev. B* 84, 235108 (2011).

[12] Sentef, M.A., Claassen, M., Kemper, A.F., Moritz, B., Oka, T., Freericks, J.K. & Devereaux, T.P. Theory of Floquet band formation and local pseudospin textures in pump-probe photoemission of graphene. *Nature Comm.* 6, 7047 (2015).

[13] Xiao, D., Liu, G.-B., Feng, W., Xu, X. & Yao, W. Coupled spin and valley physics in monolayers of mos2 and other group-vi dichalcogenides. *Phys. Rev. Lett.* 108, 196802 (2012).

[14] Tahir, M., Manchon, A. & Schwingenschlögl, U. Photoinduced quantum spin and valley Hall effects, and orbital magnetization in monolayer MoS_2. *Phys. Rev. B* 90, 125438 (2014).

[15] Bromley, R.A., Murray, R.B. & Yoffe, A.D. The band structures of some transition metal dichalcogenides. III. group via: Trigonal prism materials. *J. of Physics C: Solid State Phys.* 5, 759 (1972).

[16] Mattheiss, L.F. Band structures of transition-metal-dichalcogenide layer compounds. *Phys. Rev. B* 8, 3719–3740 (1973).

[17] Feng, W. *et al.* Intrinsic spin hall effect in monolayers of group-vi dichalcogenides: A first-principles study. *Phys. Rev. B* 86, 165108 (2012).

[18] Shan, W.-Y., Lu, H.-Z. & Xiao, D. Spin hall effect in spin-valley coupled monolayers of transition metal dichalcogenides. *Phys. Rev. B* 88, 125301 (2013).

[19] Yu, H., Wu, Y., Liu, G.-B., Xu, X. & Yao, W. Nonlinear valley and spin currents from fermi pocket anisotropy in 2d crystals. *Phys. Rev. Lett.* 113, 156603 (2014).

[20] Shan, W.-Y., Zhou, J. & Xiao, D. Optical generation and detection of pure valley current in monolayer transition-metal dichalcogenides. *Phys. Rev. B* 91, 035402 (2015).

[21] Muniz, R.A. & Sipe, J.E. All-optical injection of charge, spin, and valley currents in monolayer transition-metal dichalcogenides. *Phys. Rev. B* 91, 085404 (2015).

[22] Kogan,E., Nazarov, V.U., Silkin, V.M. & Kaveh, M. Energy bands in graphene: Comparison between the tight-binding model and ab initio calculations. *Phys. Rev. B* 89, 165430 (2014).

[23] Zahid, F., Liu, L., Zhu, Y., Wang, J. & Guo, H. A generic tight-binding model for monolayer, bilayer and bulk MoS$_2$. *AIP Advances* 3, 052111 (2013).

[24] Cappelluti, E., Roldán, R., Silva-Guillén, J.A., Ordejón, P. & Guinea, F. Tight-binding model and direct-gap/indirect-gap transition in single-layer and multilayer MoS$_2$. *Phys. Rev. B* 88, 075409 (2013).

[25] Rostami, H., Moghaddam, A.G. & Asgari, R. Effective lattice hamiltonian for monolayer mos2: Tailoring electronic structure with perpendicular electric and magnetic fields. *Phys. Rev. B* 88, 085440 (2013).

[26] Liu, G.-B., Shan, W.-Y., Yao, Y., Yao, W. & Xiao, D. Three-band tight-binding model for monolayers of group-vib transition metal dichalcogenides. *Phys. Rev. B* 88, 085433 (2013).

[27] Winkler, R., Papadakis, S.J., De Poortere, E.P. & Shayegan, M. *Spin-Orbit Coupling in Two-Dimensional Electron and Hole Systems*, volume 41. Springer (2003).

[28] Rudner, M.S., Lindner, N.H., Berg, E. & Levin, M. Anomalous edge states and the bulk-edge correspondence for periodically driven two-dimensional systems. *Phys. Rev. X* 3, 031005 (2013).

[29] Liu, C.-X., Qi, X.-L., Dai, X., Fang, Z. & Zhang, S.-C. Quantum anomalous hall effect in $Hg_{1-y}Mn_yTe$ quantum wells. *Phys. Rev. Lett.* 101, 146802 (2008).

Methods

***ab initio* Calculations** *ab initio* calculations were performed in the framework of the Perdew-Burke-Ernzerhof (PBE) type generalized gradient approximation (GGA) of density functional theory (DFT) using the full-potential linearized augmented plane wave method implemented in Wien2k [30]. We consider a single monolayer of WS_2 with a 30rA vacuum space perpendicular to the layer along the z-direction. The in-plane lattice constant and the S position have been relaxed by optimization of the total energy and total force, respectively. For electronic structure calculations, we utilized a $15\times15\times1$ k-space grid. Momentum matrix element calculations were performed using the OPTIC package implemented in Wien2k, with a $60\times60\times1$ k-space grid. Maximally-localized Wannier functions (MLWFs) for the five W $5d$ orbitals were obtained using wien2wannier [31] and Wannier90 [32] with initial projections set to the spherical harmonics Y_{2m} (m = -2, -1, 0, 1, 2). Due to the symmetry of the hexagonal lattice, the calculated Hamiltonian in the new Wannier basis naturally decouples into the two standard subspaces { $d_{x^2-y^2} \pm i\, d_{2xy}$, $d_{3z^2-r^2}$ } and { $d_{xz} \pm id_{yz}$ }.

Floquet theory of the single-particle spectrum on a ribbon Floquet theory captures the effective steady states that arise from a time-dependent (quasi-)periodic modulation. Consider a Hamiltonian $\hat{H}(t) = \hat{H}(t + \frac{2\pi}{\Omega})$ with a periodic time dependence with frequency Ω. Then, solutions of the time-dependent Schrödinger equation for $\hat{H}(t)$ can be written as $\Phi(t) = e^{i\epsilon t} \sum_m u_m e^{im\Omega t}$, where ϵ is the Floquet quasi-energy, and u_m are Fourier coefficients of the time-periodic part of the wave function. Substitution of $\Phi(t)$ into Schrödinger's equation recasts the time-dependent problem as an effective time-independent Floquet problem: the Floquet states can be found by finding eigenstates of

the Floquet Hamiltonian

$$\hat{H}_F = \sum_{mm'} \left[\hat{H}_{m-m'} + m\Omega\delta_{m-m'} \right] |m\rangle\langle m'| , \tag{3}$$

where $\hat{H}_{m-m'} = \frac{\Omega}{2\pi} \int_0^{2\pi/\Omega} \hat{H}(t)e^{i(m-m')\Omega t}$ are the Fourier expansion coefficients of $\hat{H}(t)$. If the original Hamiltonian has a static eigenbasis $|\alpha\rangle$, then the eigenstates of $\hat{H}_F$ can be written as $|\lambda\rangle = \sum_m u_{m\alpha}^{(\lambda)} |\alpha\rangle \otimes |m\rangle$, with the original time-dependent eigenstates of $\hat{H}(t)$ becoming $|\lambda(t)\rangle = e^{i\epsilon_\lambda t} \sum_m u_{m\alpha}^{(\lambda)} e^{im\Omega t} |\alpha\rangle$. The next step is to connect back to observables of the original fermion operators. In the main text, we consider the spectral function

$$A(\omega, x) = -2\text{Im}\left\{ \frac{\Omega}{2\pi} \sum_{\alpha\alpha'} \int_0^{2\pi/\Omega} dT \int_{-\infty}^{\infty} d\tau e^{i\omega\tau} G_{\alpha\alpha'}^R\left(x, T + \frac{\tau}{2}; x, T - \frac{\tau}{2}\right) \right\} \tag{4}$$

where $G_{\alpha\alpha'}^R(x, t; x', t') = -i\theta(t-t') \left\langle \left\{ \Psi_\alpha(x, t), \ \Psi_{\alpha'}^\dagger(x', t') \right\} \right\rangle$ is the retarded Green's function. Rewriting the fermion operators $\Psi_\alpha(x, t)$ in Floquet basis, one finally arrives at the Floquet spectral function

$$A(\omega, x) \sim \sum_{m\lambda\alpha} \left| u_{mx\alpha}^{(\lambda)} \right|^2 \frac{\Gamma}{(\omega - \epsilon_\lambda + m\Omega)^2 + \Gamma^2} \tag{5}$$

where Γ is a phenomenological broadening of the spectrum.

Floquet k.p Theory and Effective Hamiltonians at $\mathbf{K}, \mathbf{K}'$ Here, we describe in detail the derivation of the effective Hamiltonians (1) and (2) at $\mathbf{K}$ and $\mathbf{K}'$ that capture the Floquet-Bloch band inversions for red and blue detunings. We take into account the full *ab initio* problem including spin-orbit coupling (SOC). For brevity, and consistent with the main text, we employ C_{3h} single group IRs $A', E', \bar{E}'$, and ignore weak spin-flip terms such that the effect of SOC enters as a Zeeman-like shift on spin $\uparrow_z, \downarrow_z$ bands. However, as discussed in the supplementary information, the crystal double group dictates that the discussion below remains the same under inclusion of spin-flip scattering, and

the full SOC problem can be readily recovered merely by replacing the single-group by the appropriate double IRs [Supplementary Information].

At $\mathbf{K}$ (and equivalently at $\mathbf{K}'$), a Floquet-Bloch eigenbasis follows from a solution of the the time-dependent Hamiltonian

$$\hat{H}_0(t) = \frac{1}{2m_0}[\hat{\mathbf{p}} + \mathbf{K} + e\mathbf{A}(t)]^2 + V(\mathbf{r}) + \frac{\hbar}{4m_0^2 c_0^2}[\hat{\mathbf{p}} + e\mathbf{A}(t)] \cdot \hat{\boldsymbol{\sigma}} \times \boldsymbol{\nabla} V(\mathbf{r}) \qquad (6)$$

where $A(t) = A_0[\cos(\Omega t), \ \sin(\Omega t)]^\top$ is the circularly-polarized pump field. Consider a single spin manifold (see supplementary info for the double group identifications in the full SOC problem): in Floquet language, finding the steady-state eigenbasis at $\mathbf{K}, \mathbf{K}'$ amounts to determining the eigenstates of the time-independent Floquet Hamiltonian:

$$\begin{aligned}
\hat{H}_{0F} = & \sum_{mn\alpha} \left(\epsilon_{n\alpha} + m\Omega + \frac{e^2 A_0^2}{2m_0} \right) |m; n\alpha\rangle\langle m; n\alpha| \\
& + A_0 \sum_{mnn'} \left(g_{nn'}^{A'E'} |m+1; n, A'\rangle\langle m; n', E'| \right. \\
& \qquad + g_{nn'}^{\bar{E}'A'} |m+1; n, \bar{E}'\rangle\langle m; n', A'| \\
& \qquad \left. + g_{nn'}^{E'\bar{E}'} |m+1; n, E'\rangle\langle m; n', \bar{E}'| + \text{h.c.} \right)
\end{aligned} \qquad (7)$$

Here, m is the Floquet index; n, α index the n$^\text{th}$ band in the C_{3h} IRs $\alpha = A', E', \bar{E}'$, and $g_{nn'}^{\alpha\alpha'}$ are the allowed dipole transitions matrix elements of $\hat{\boldsymbol{\pi}} = \hat{\mathbf{p}} + \mathbf{K} + \frac{\hbar}{4m_0^2 c_0^2}\hat{\boldsymbol{\sigma}} \times \boldsymbol{\nabla} V(\mathbf{r})$ that can be obtained from *ab initio* calculations.

Having determined the new eigenbasis that admixes different Floquet side bands and IRs of C_{3h}, deviations in momentum away from $\mathbf{K}$ can be treated as a perturbation:

$$\begin{aligned}
\hat{H}' = & \sum_{mn\alpha} \frac{A_0}{2} k_- |m+1; n, \alpha\rangle\langle m; n, \alpha| + \text{h.c.} \\
& + k_+ \sum_{mnn'} \left(g_{nn'}^{A'E'} |m; n, A'\rangle\langle m; n', E'| \right. \\
& \qquad + g_{nn'}^{\bar{E}'A'} |m; n, \bar{E}'\rangle\langle m; n', A'| \\
& \qquad \left. + g_{nn'}^{E'\bar{E}'} |m; n, E'\rangle\langle m; n', \bar{E}'| + \text{h.c.} \right)
\end{aligned} \qquad (8)$$

16

where $k_{\pm} = k_x \pm ik_y$. An effective two-band Hamiltonian description of high-symmetry points now follows from canonical Löwdin partitioning of $\hat{H}'$ in the eigenbasis of $\hat{H}_{0F}$, as described in the main text.

Importantly, the inclusion of full spin-orbit coupling does not qualitatively alter these conclusions. First, spin-flip terms only weakly admix E'' bands of opposite spin [35,36]; however, the full crystal double group $\bar{C}_{3h}$ again decomposes into two spin-orbital manifold with equivalent selection rules and effective physics [Supplementary Material]. Second, the valley Zeeman shift simply leads to a shift of the relevant resonance energies. Similarly, while monolayer TMDCs have been shown to give rise to large excitonic binding energies [33,34], in the context of our work their role is confined to shifting the relevant resonance energies, given appropriate tuning of the pump frequency.

References and Notes (Methods)

30. Blaha, P., Schwarz, K., Madsen, G.K.H., Kvasnicka, D. & Luitz, J. *Wien2K: An augmented plane wave and local orbitals program for calculating crystal properties*, Technische Universität Wien, Austria (2001).

31. Kuneš, J.*et al.* Wien2wannier: From linearized augmented plane waves to maximally localized Wannier functions. *Comp. Phys. Comm.* 181, 1888 (2010).

32. Mostofi, A.A. *et al.* wannier90: A Tool for obtaining maximally-localised Wannier

functions. *Comp. Phys. Comm.* 178, 685 (2008).

33. Chernikov, A., Berkelbach, T.C., Hill, H.M., Rigosi, A., Li, Y., Aslan, O.B., Reichman, D.R., Hybertsen, M.S. & Heinz, T.F. Exciton binding energy and nonhydrogenic Rydberg series in monolayer WS_2. *Phys. Rev. Lett.* 113, 076802 (2014).

34. Zhu, B., Chen, X. & Cui, X. Exciton Binding Energy of Monolayer WS_2. *Sci. Rep.* 5, 9218 (2015).

35. Kormányos, A. *et al.* Monolayer MoS_2: Trigonal warping, the Γ valley, and spin-orbit coupling effects. *Phys. Rev. B* 88, 045416 (2013).

36. Gibertini, M., Pellegrino, F.M.D., Marzari, N. & Polini, M. Spin-resolved optical conductivity of two-dimensional group-VIB transition-metal dichalcogenides. *Phys. Rev. B* 90, 245411 (2014).
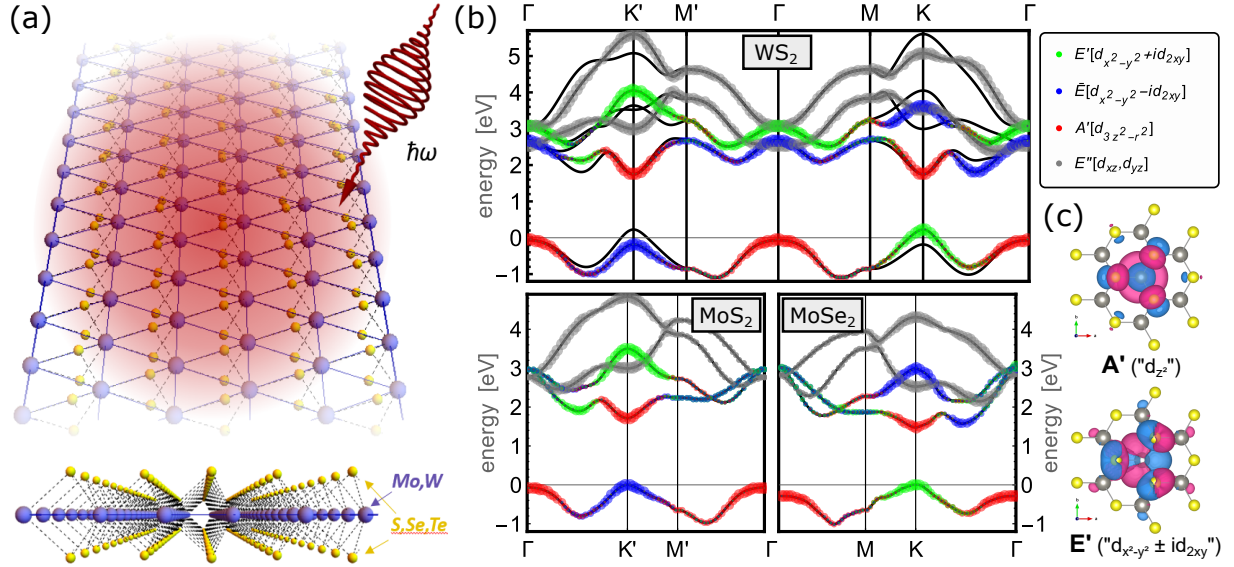
Figure 1: (a) Setup: a circularly-polarized pump beam irradiates a monolayer transition-metal dichalcogenide ribbon. (b) Band structure and orbital content for MoS_2 and $MoSe_2$, as well as WS_2 with spin-orbit coupling, determined from *ab initio* DFT calculations and downfolding onto localized Wannier orbitals. (c) Isosurfaces highlight that the effective Wannier orbitals for WS_2, while localized on W, take into account orbital content extending to the S atoms as well as neighboring W atoms.
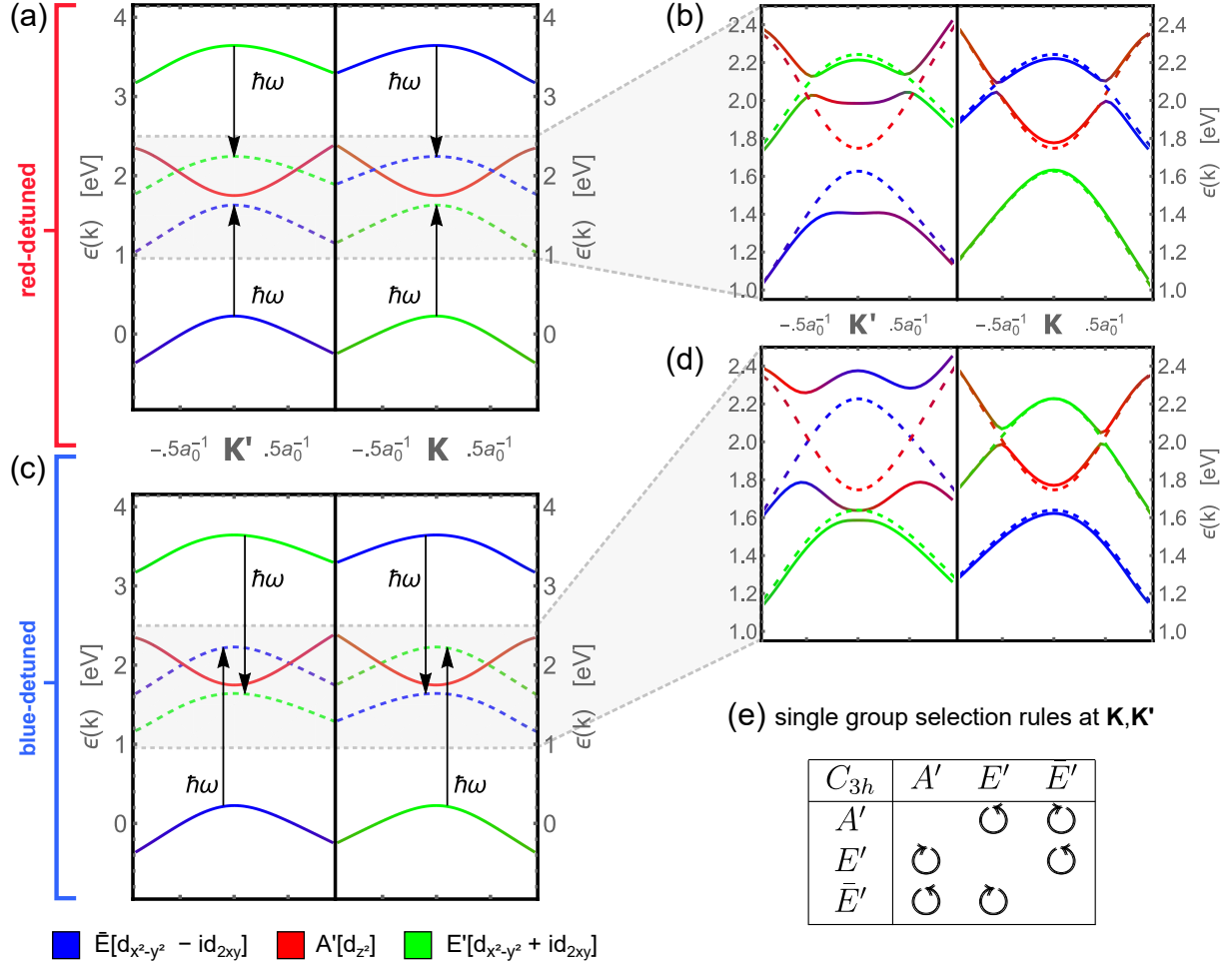
Figure 2: Photon-dressed *ab initio* Floquet bands of Kramer's pair $\mathbf{K}$, $\mathbf{K'}$, for red (a,b) and blue (c,d) detuning. A red-detuned (blue-detuned) pump generically brings into resonance a ring of states of the E' higher-energy band ($\bar{E}'$ valence band) with the A' conduction band, while leaving the valence band (higher-energy band) off-resonant. Electric dipole coupling mixes the equilibrium orbital characters at $\mathbf{K}, \mathbf{K'}$ while lifting degeneracies between the conduction band and photon-dressed copies of the other bands (b,d). The ensuing photo-induced hybridization gap leads to topologically non-trivial band inversion at a single valley. (e) The corresponding C_{3h} single group selection rules at $\mathbf{K}, \mathbf{K'}$ for circular polarization [see supplementary material for a double group generalization].
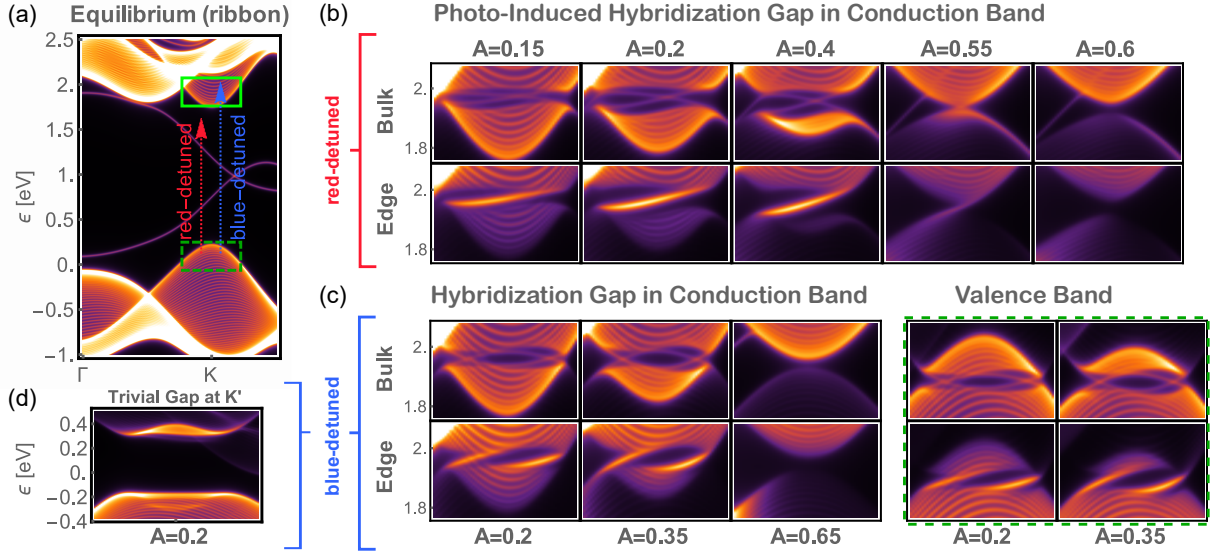
Figure 3: Single-particle spectra for a WS$_2$ ribbon irradiated with circularly-polarized light. (a) In equilibrium, the ribbon hosts two trivial edge states localized at opposing edges. (b) A red-detuned pump field induces a hybridization gap at the bottom of the conduction band, which scales linearly in A until closing again at a critical pump strength. (c) A blue detuned pump couples the equilibrium valence and conduction bands, inducing gaps both at the bottom of the conduction and top of the valence band, each hosting *two* chiral edge modes. (d) Hybridization gaps at the opposite valley $\mathbf{K}'$ lead merely to a trivial band inversion, depicted here for the top of the valence band for blue detuning.

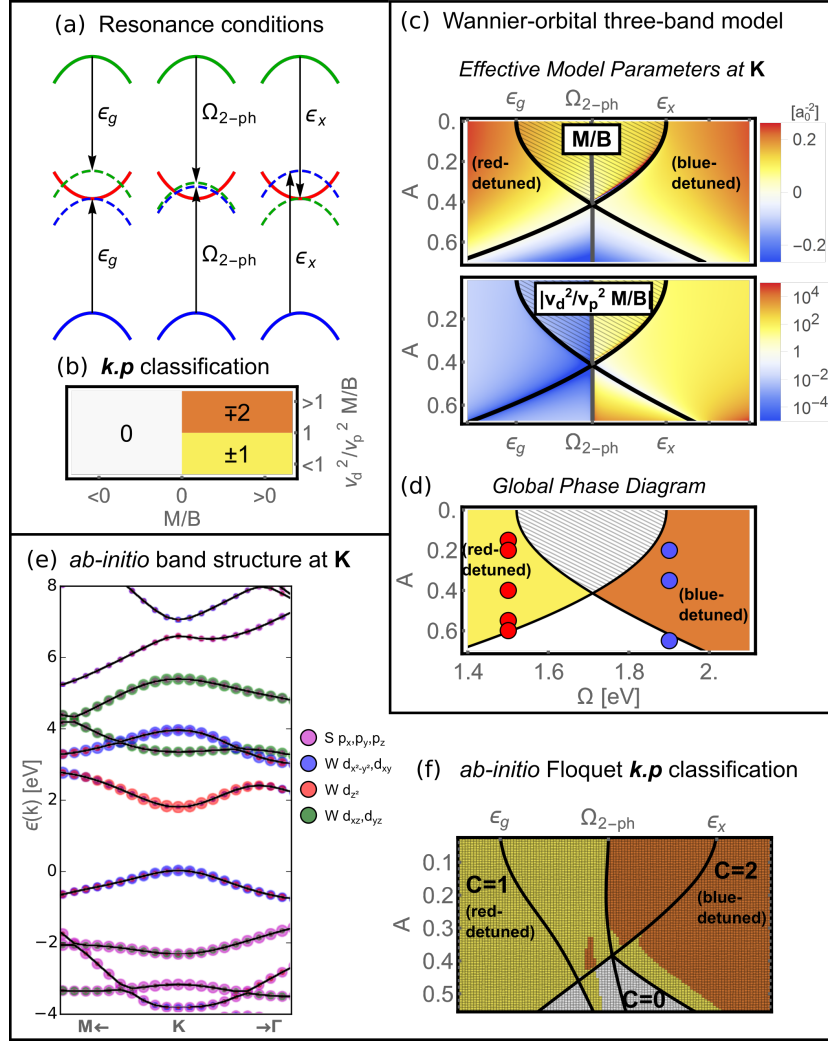Figure 4: (a) The relevant resonances when moving from red to blue detuning. (c) Effective **k.p** parameterization of the band inversion at **K** starting from the three-orbital Wannier tight-binding model. The sign of M/B a_0^2 is negative in the inverted regime, whereas the system transitions from one (red-detuned) to two (blue-detuned) chiral edge modes when $\left| (v_d/v_p)^2 \frac{M}{B} \right| > 1$, as depicted schematically in (b). The effective **k.p** model accounts for the Floquet state adiabatically derived from the original conduction band, as well as the Floquet state deriving from the valence band dressed by one absorbed photon, for red detuning, or from the higher-energy E' band dressed by one emitted photon, for blue detuning. This entails the sharp transition when sweeping the pump frequency across the two-photon resonance between VB and XB (a). Within the shaded areas, all three bands come into resonance. (d) A corresponding numerical calculation of the global Chern number of the tight-binding model mirrors the **k.p** analysis. To correctly account for the effects of multi-photon processes involving deep core levels or higher-energy bands, we start from a first-principles description of 185 bands at **K** (e) and recompute the effective Floquet two-band model and phase diagram of Fig. 2 in *ab initio* Floquet **k.p** theory. The resulting phase diagram (f) remains qualitatively the same, suggesting that the photo-induction of one or two chiral edge modes for appropriate tuning of the pump laser is robust to multi-photon processes at weak pump fields.

Supplementary Material

Symmetry Analysis and the Role of Spin-Orbit Coupling

In the absence of spin-orbit coupling (SOC), the relevant bands near $\mathbf{K}, \mathbf{K}'$ can be classified according to the single-group irreducible representations (IRs) of the point group C_{3h}, denoted $A', E', \bar{E}', E'', \bar{E}''$ [15, 16]. The corresponding character table and relevant invariants are depicted in Tbl. 2. As discussed in the main text, reflection symmetry σ_h guarantees that bands $A', E', \bar{E}'$ remain decoupled from $E'', \bar{E}'$ across the entire Brillouin zone [13, 23, 24, 25, 26], and the analysis can therefore be constrained to three relevant bands $A', E', \bar{E}'$ only. In 2H monolayer TMDCs, the conduction band transforms as A' and is dominantly composed of the transition metal $d_{3z^2-r^2}$ orbital, whereas the valence and relevant higher-energy band transform as $E', \bar{E}'$ with a dominant contribution of $d_{x^2-y^2} \pm id_{2xy}$ orbitals. Furthermore, spin z is a good quantum number.

In equilibrium, the band structure can be expanded in $\mathbf{k}$ around $\mathbf{K}, \mathbf{K}'$ by starting from Hamiltonian

$$\hat{H} = \hat{H}_0 + \hat{H}_{SOC} + \hat{H}_{\mathbf{k}} \tag{S1}$$

where

$$\hat{H}_0 = \frac{1}{2m_0}\hat{\mathbf{p}}^2 + V(\mathbf{r}) \tag{S2}$$

$$\hat{H}_{SOC} = \frac{\hbar}{4m_0^2 c_0^2}\hat{\mathbf{p}} \cdot \hat{\boldsymbol{\sigma}} \times \boldsymbol{\nabla} V(\mathbf{r}) \tag{S3}$$

$$\hat{H}_{\mathbf{k}} = \frac{\hbar^2 \mathbf{k}^2}{2m_0} + \frac{\hbar}{2m_0}\mathbf{k} \cdot \left[\hat{\mathbf{p}} + \frac{\hbar}{4m_0^2 c_0^2}\hat{\boldsymbol{\sigma}} \times \boldsymbol{\nabla} V(\mathbf{r})\right] \tag{S4}$$

Here, $\hat{\boldsymbol{\sigma}}$ are the Pauli matrices, and $V(\mathbf{r})$ is the crystal potential.

The role of SOC can now be understood in two complementary ways, by either considering the eigenstates of $\hat{H}_0$ as IRs of the C_{3h} single group and treating SOC as a

perturbation, or by starting from the true Bloch eigenstates of $\hat{H}_0 + \hat{H}_{SOC}$ at $\mathbf{K}, \mathbf{K}'$, as IRs of the $\bar{C}_{3h}$ double group. In the former case, the eigenstates of $\hat{H}_0$ are spin-z eigenstates with a given single-group IR, namely $|A'[d_{3z^2-r^2}], \sigma\rangle$, $|E'[d_{x^2-y^2} + id_{2xy}], \sigma\rangle$ and $\left|\bar{E}'[d_{x^2-y^2} - id_{2xy}], \sigma\right\rangle$ with $\sigma =\uparrow_z, \downarrow_z$. To understand the effect of SOC, it is useful to decompose $\hat{H}_{SOC}, \hat{H}'_{\mathbf{k}}$:

$$\hat{H}_{SOC}^z = \hat{\sigma}_z \left[\hat{p}_x \partial_y - \hat{p}_y \partial_x\right] V(\mathbf{r}) \tag{S5}$$

$$\hat{H}_{SOC}^{\uparrow\downarrow} = 2i\hat{\sigma}^- \left[\hat{p}_z \partial_+ V(\mathbf{r}) - \hat{p}_+ \partial_z V(\mathbf{r})\right] + \text{h.c.} \tag{S6}$$

$$\hat{H}_{\mathbf{k}}^z = \frac{\hbar^2 \mathbf{k}^2}{2m_0} + \frac{\hbar}{2m_0} \left[k_+ \cdot \left(\hat{\mathbf{p}} - i\hat{\sigma}_z \frac{\hbar}{4m_0^2 c_0^2} \partial_- V(\mathbf{r})\right) + \text{h.c.}\right] \tag{S7}$$

$$\hat{H}_{\mathbf{k}}^{\uparrow\downarrow} = \frac{\hbar}{2m_0} k_+ \cdot \left(\hat{\mathbf{p}} + i\hat{\sigma}_- \frac{\hbar}{4m_0^2 c_0^2} \partial_z V(\mathbf{r})\right) + \text{h.c.} \tag{S8}$$

Here, $\hat{H}_{SOC}^z$ transforms as A' and acts as a mere Zeeman shift, whereas the spin-flip contribution $\hat{H}_{SOC}^{\uparrow\downarrow}$ transforms as $E'', \bar{E}''$ and hence couples states with opposite parity under σ_h. The latter entails a mixing between conduction band state $|A', \sigma\rangle$ and $\left|E''(\bar{E}''), -\sigma\right\rangle$ as well as between the higher-energy conduction band $\left|\bar{E}', \uparrow\right\rangle$ and $|E'', \downarrow\rangle$ while leaving the opposite spin $\left|\bar{E}', \downarrow\right\rangle$ unmixed. However, this mixing of $\uparrow_z, \downarrow_z$ states is suppressed as the energy difference between the A', E' and E'' bands is larger than the spin-orbit coupling. The SOC at $\mathbf{K}, \mathbf{K}'$ can therefore be well-captured as an effective Zeeman shift [24, 26, 17] while approximately leaving spin as a good quantum number [35, 36]. Away from $\mathbf{K}, \mathbf{K}'$, $\hat{H}_{\mathbf{k}}^z$ transforms as $E', \bar{E}'$ and imparts an additional momentum-dependent Zeeman shift. Conversely, $\hat{H}_{\mathbf{k}}^{\uparrow\downarrow}$ transforms as A'', which does not couple the A' states of the original conduction band while weakly mixing the E', E'' bands.

Consider now the double group, with its character table given in Tbl. 2. Spin-flip mixing with the $E'', \bar{E}''$ bands necessarily reduces the number of band IRs from 5 IRs $\times 2$ spin orientations, to 6 double-group IRs. These again decompose into into two manifolds denoted $\Uparrow, \Downarrow$ that remain decoupled over the entire Brillouin zone. The identification

24

of band states with single group and double group IRs is given in Tbl. 2(b). Note that the states listed are not an eigenbasis of $\hat{H}_0 + \hat{H}_{SOC}$: instead, the true eigenbasis will be a superposition of states of equal double-group IR, governed by the strength of SOC. At $\mathbf{K}, \mathbf{K}'$, one can immediately deduce that the eigenbasis entails mixing of $|d_{3z^2-r^2}, \sigma\rangle$ and $|d_{xz+\sigma\cdot iyz}, -\sigma\rangle$, of $|d_{x^2-y^2+2ixy} + id_{2xy}, \uparrow\rangle$ and $|d_{xz-iyz}, \downarrow\rangle$, and of $|d_{xz+iyz}, \uparrow\rangle$ and $|d_{x^2-y^2} - id_{2ixy}, \downarrow\rangle$, while leaving states $|d_{x^2-y^2} - id_{2xy}, \uparrow\rangle$ and $|d_{x^2-y^2} + id_{2xy}, \downarrow\rangle$ unmixed and as proper eigenstates of $\hat{H}_0 + \hat{H}_{SOC}$.

Here, the $\mathbf{k.p}$ perturbation transforms as Γ_2, Γ_3 and couples the three $\Uparrow$ IRs $\Gamma_7, \Gamma_{10}, \Gamma_{11}$ ($\Downarrow$ IRs $\Gamma_8, \Gamma_9, \Gamma_{12}$) in an equivalent manner as in the single-group case of $A', E', \bar{E}'$ without spin-orbit coupling, or with SOC but without spin-flip terms. Consequently, the selection rules of electric dipole transitions for circular polarization are exactly equivalent, as shown in Tbl. 2(c). For this reason, we chose to simply adopt the single-group notation and label the spin manifolds as $\uparrow_z, \downarrow_z$, while keeping in mind that SOC is indeed significant for certain TMDCs and enters through a one-to-one correspondence with the double group IRs and spin manifolds $\Uparrow, \Downarrow$.

Topological Classification and Pseudospin Textures

The main text classifies photo-induced topological phase transitions via local effective Floquet $\mathbf{k.p}$ Hamiltonians at $\mathbf{K}, \mathbf{K}'$. The key idea is to understand the global topology via a local classification of band inversions at $\mathbf{K}, \mathbf{K}'$, which relies on *a-priori* knowledge that 1) the Floquet spectrum is gapped globally and 2) the Berry curvature behaves benign at other high-symmetry points in the Brillouin zone. Armed with this knowledge, a complementary view of local band inversions follows from considering so-called pseudospin textures around $\mathbf{K}$ and $\mathbf{K}'$. Starting from the local Floquet $\mathbf{k.p}$ Hamiltonians $\hat{H}_{\mathbf{K}}(\mathbf{k})$ and $\hat{H}_{\mathbf{K}'}(\mathbf{k})$ of equations 3 and 4 of the main text, we can recast these in terms of pseudospin

Pauli matrices $\boldsymbol{\sigma}$:

$$\hat{H}_{\nu=\mathbf{K},\mathbf{K}'}(\mathbf{k}) = \epsilon_0(\mathbf{k}) + \epsilon(\mathbf{k})\,\hat{\mathbf{d}}_\nu(\mathbf{k})\cdot\boldsymbol{\sigma} \tag{S9}$$

Here, $\epsilon_0(\mathbf{k}) \pm \epsilon(\mathbf{k})$ is the dispersion of $\hat{H}_{\mathbf{K}}(\mathbf{k})$ or $\hat{H}_{\mathbf{K}'}(\mathbf{k})$, and $\hat{\mathbf{d}}_\nu(\mathbf{k})$ is the pseudospin vector, with $|\hat{\mathbf{d}}_\nu(\mathbf{k})| = 0$. Here, $\nu = \mathbf{K}, \mathbf{K}'$. The pseudospin vector equivalently follows from taking the expectation value $\langle\boldsymbol{\sigma}\rangle$ of the Floquet-Bloch states around $\mathbf{K}, \mathbf{K}'$.

As discussed in the main text, the band inversion at $\mathbf{K}'$ is trivial, and the pseudospin obeys $d_{\mathbf{K}}^y(\mathbf{k}) = 0$. Conversely, at $\mathbf{K}$, the pseudospin becomes

$$\hat{\mathbf{d}}_{\mathbf{K}}(\mathbf{k}) = \frac{1}{N(\mathbf{k})}\left[v_1 k_x + v_3(k_x^2 - k_y^2),\ v_1 k_y - 2v_3 k_x k_y,\ M - B|\mathbf{k}|^2\right]^\top \tag{S10}$$

with a normalization $N(\mathbf{k})$ to ensure that $|\hat{\mathbf{d}}_{\mathbf{K}}(\mathbf{k})| = 1$.

At $\mathbf{K}$, the effective Hamiltonian S9 can be viewed as a d-wave generalization of the conventional massive Dirac Hamiltonian, with an additional band mass term in analogy to the $\mathbf{k}.\mathbf{p}$ model at Γ for HgTe/CdTe quantum wells. Figure S1 depicts the pseudospin textures upon increasing v_3/v_1 to enhance trigonal distortion. $v_1 \neq 0, v_3 = 0$ recovers the conventional massive Dirac fermion with a quadratic band mass term; here, the pseudospin has a p-wave winding around $\mathbf{K}'$ and the Chern number becomes $C = 1$. In the opposite limit $v_1 = 0, v_3 \neq 0$, the pseudospin acquires a d-wave winding around $\mathbf{K}$. Here, since the band mass term is quadratic only, the winding in $d^x(\mathbf{k}), d^y(\mathbf{k})$ persists in principle to $k \to \infty$. Given the knowledge that the band structure is gapped globally and that the band inversion should be confined to high-symmetry points, this behavior is an artifact of the lower-order $\mathbf{k}.\mathbf{p}$ expansion.

More rigorously, quantization of the integral $\mathcal{C} = \frac{1}{2\pi}\int_{\mathbb{R}^2} d\mathbf{k}\mathcal{F}(\mathbf{k})$ necessitates a compactification of k-space $\mathbb{R}^2$ to a non-contractible manifold. This can be motivated as follows: Since the Floquet $\mathbf{k}.\mathbf{p}$ theory can be expected to faithfully represent the physics only in the close vicinity around $\mathbf{K}$, momenta $\mathbf{k}$ far away from $\mathbf{K}$ should not affect $\mathcal{C}$.

This can be enforced rigorously by adding to $\hat{H}$ an infinitesimal rotationally-symmetric regularizer $-\eta B' \hat{\sigma}_z |\mathbf{k}|^4$ with $\eta \to 0$, leading to:

$$\hat{\mathbf{d}}_{\mathbf{K}'}^{(\text{reg})}(\mathbf{k}) = \frac{1}{N(\mathbf{k})} \left[v_1 k_x + v_3(k_x^2 - k_y^2), \ v_1 k_y - 2v_3 k_x k_y, \ M - B|\mathbf{k}|^2(1 + \eta |\mathbf{k}|^2) \right]^\top \quad (\text{S11})$$

It follows that the unit vector $\hat{\mathbf{d}}_{\mathbf{K}'}^{(\text{reg})}(|\mathbf{k}| \to \infty) = -\text{sgn}(B)\hat{e}_z$ does not depend on the polar angle θ of $\mathbf{k}$, and $\mathbb{R}^2$ can be compactified to a sphere S_2 by identifying ∞ with the north pole without loss of information. The choice $\hat{\sigma}_z$ of the regularizer is motivated by noting that $|B| \gg |v_3|$ for any choice of pump field entails that $\hat{\mathbf{d}}(|\mathbf{k}| \to \infty) \sim -\text{sgn}(B)\hat{e}_z + \frac{v_3}{|B|}[\cos(2\theta)\hat{e}_x - \sin(2\theta)\hat{e}_y]$ already approximately points in the z-direction.

The band inversion can be seen clearly by looking at the behavior of $d^z(\mathbf{k})$ close to $\mathbf{K}$, which switches sign when going from $\mathbf{k} = 0$ to $\mathbf{k} \to \infty$. The intermediate regime of p-d-wave winding leads to a distorted pseudospin texture when looking at the close vicinity of $\mathbf{K}$, whereas a d-wave (or p-wave) texture is retained at large $\mathbf{k}$ to arrive at a $C = 2$ or $C = 1$ phase.

Strong Pumping and Inversion of the Equilibrium Band Gap

Discussions on photo-induced chiral edge states have focused so far solely on dynamically-generated gaps *within* the equilibrium conduction and valence bands, since a sizeable energy scale $\sim 1.5eV$ in WS_2 protects the equilibrium band gap from closing for weak pump fields. This picture changes conceivably when approaching the regime of Wannier-Stark physics at significantly higher pump strength. In the high-frequency limit, broken time-reversal symmetry then bestows an optical Stark shift of equal and opposite magnitude on $\mathbf{K}$ and $\mathbf{K}'$, that bridges the equilibrium band gap at a critical field strength A. The gap closes and reopens at $\mathbf{K}'$ to eliminate one branch of the trivial equilibrium edge states, leaving a single chiral edge state to bridge the Floquet-Bloch band gap at $\mathbf{K}$, as depicted in Fig. 2(a). Upon even further increase of A, the gap finally closes and reopens

at Γ, returning to a trivial regime without chiral edge modes. Naïvely, the flattening of the bands upon crossover to Wannier-Stark ladders at increasing pump strengths A or decreasing frequencies Ω suggests that one should not expect to continue attributing special significance to the original high-symmetry points in this regime. Nevertheless, the system can undergo a series of gap closings confined to $\mathbf{K}, \mathbf{K'}, \Gamma$ upon further decrease of Ω. The associated topological transitions change the Floquet Chern number by ± 1, leading to a mosaic of photo-induced topological phases at high pump intensities. In addition, gap closures occur near the second conduction-band minimum $\mathbf{Q}$ in WS_2. As this is not a high-symmetry point, C_3 rotation symmetry dictates that the gap must instead close simultaneously at three distinct points in the Brillouin zone, changing the Chern number by ± 3. We verified the corresponding phase diagram in Fig. 2(b) by numerically evaluating the Floquet Chern number.

Table S1: Single group C_{3h}

(a) C_{3h} single group character table, with $\Omega = \exp(2\pi i/3)$.

	E	C_3^+	C_3^-	σ_h	S_3^+	S_3^-	invariants
A'	1	1	1	1	1	1	$x^2 + y^2,\ z^2$
E'	1	Ω	$\bar{\Omega}$	1	Ω	$\bar{\Omega}$	$x - iy,\ (x+iy)^2$
$\bar{E}'$	1	$\bar{\Omega}$	Ω	1	$\bar{\Omega}$	Ω	$x + iy,\ (x-iy)^2$
A''	1	1	1	-1	-1	-1	z
E''	1	Ω	$\bar{\Omega}$	-1	$-\Omega$	$-\bar{\Omega}$	$(x-iy)z$
$\bar{E}''$	1	$\bar{\Omega}$	Ω	-1	$-\bar{\Omega}$	$-\Omega$	$(x+iy)z$

(b) Selection rules for electric dipole transitions, for circular polarization

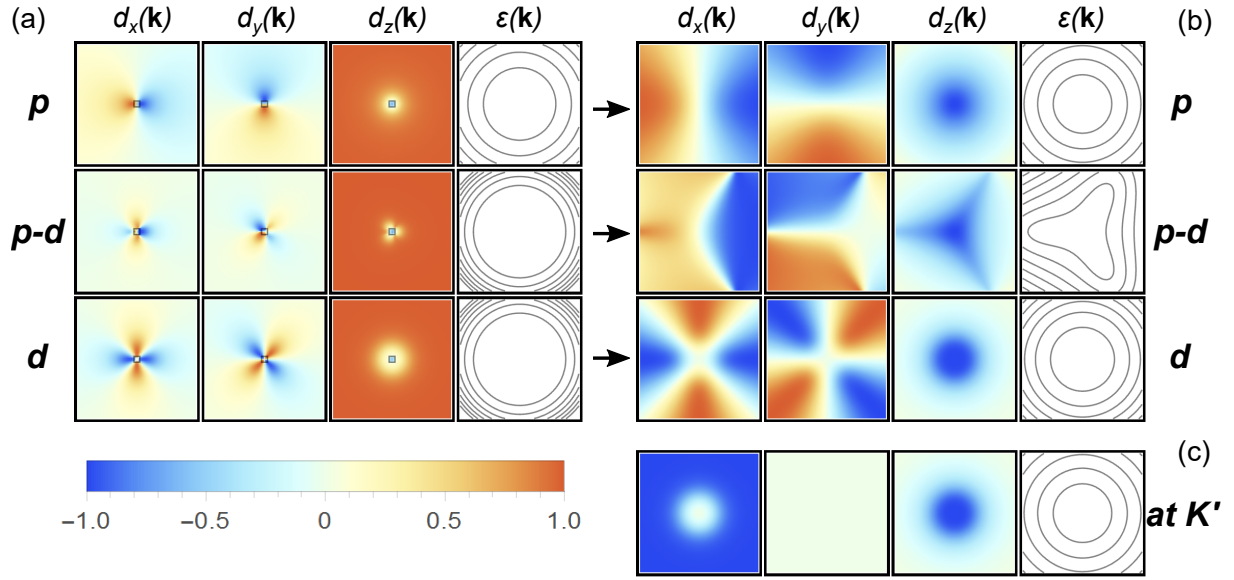|	A'	E'	$\bar{E}'$
A'		↻	↺
E'	↺		↺
$\bar{E}'$	↻	↻	

Figure S1: Floquet-Bloch pseudospin textures at $\mathbf{K}$ and $\mathbf{K}'$. (a) At $\mathbf{K}$ the pseudospin texture interpolates between p-wave ($v_1 \neq 0, v_3 = 0$) and d-wave ($v_1 = 0, v_3 \neq 0$) winding upon increase of trigonal distortion. Given *a-priori* knowledge that the band structure remains gapped globally, a topological invariant can be assigned by introducing a regularizer η that ensures that the pseudospin points into the z direction for $k \to \infty$ and the $\mathbf{k}$-space manifold can thus be compatified to a sphere. Trigonal distortion is seen clearly when zooming into the vicinity of the $\mathbf{K}$ point, as depicted in (b). Here, little information can be gleaned from the intermediate p-d wave texture, however globally a d-wave winding appears as seen in (a). At $\mathbf{K}'$, the pseudospin is trivial, with the y-component always zero, depicted in (c).

Table S2: Double group $\bar{C}_{3h}$

(a) $\bar{C}_{3h}$ double group character table, with complex characters $\Omega = \exp(2\pi i/3)$.

	E	C_3^+	C_3^-	σ_h	S_3^+	S_3^-	$\bar{E}$	$\bar{C}_3^+$	$\bar{C}_3^-$	$\bar{\sigma}_h$	$\bar{S}_3^+$	$\bar{S}_3^-$	invariants
Γ_1	1	1	1	1	1	1	1	1	1	1	1	1	x^2+y^2, z^2
Γ_2	1	Ω	$\bar{\Omega}$	1	Ω	$\bar{\Omega}$	1	Ω	$\bar{\Omega}$	1	Ω	$\bar{\Omega}$	$x-iy, (x+iy)^2$
Γ_3	1	$\bar{\Omega}$	Ω	1	$\bar{\Omega}$	Ω	1	$\bar{\Omega}$	Ω	1	$\bar{\Omega}$	Ω	$x+iy, (x-iy)^2$
Γ_4	1	1	1	-1	-1	-1	1	1	1	-1	-1	-1	z
Γ_5	1	Ω	$\bar{\Omega}$	-1	$-\Omega$	$-\bar{\Omega}$	1	Ω	$\bar{\Omega}$	-1	$-\Omega$	$-\bar{\Omega}$	$(x-iy)z$
Γ_6	1	$\bar{\Omega}$	Ω	-1	$-\bar{\Omega}$	$-\Omega$	1	$\bar{\Omega}$	Ω	-1	$-\bar{\Omega}$	$-\Omega$	$(x+iy)z$
Γ_7	1	$-\Omega$	$-\bar{\Omega}$	i	$-i\Omega$	$i\bar{\Omega}$	-1	Ω	$\bar{\Omega}$	$-i$	$i\Omega$	$-i\bar{\Omega}$	$\uparrow_z$
Γ_8	1	$-\bar{\Omega}$	$-\Omega$	$-i$	$i\bar{\Omega}$	$-i\Omega$	-1	$\bar{\Omega}$	Ω	i	$-i\bar{\Omega}$	$i\Omega$	$\downarrow_z$
Γ_9	1	$-\Omega$	$-\bar{\Omega}$	$-i$	$i\Omega$	$-i\bar{\Omega}$	-1	Ω	$\bar{\Omega}$	i	$-i\Omega$	$i\bar{\Omega}$	
Γ_{10}	1	$-\bar{\Omega}$	$-\Omega$	i	$-i\bar{\Omega}$	$i\Omega$	-1	$\bar{\Omega}$	Ω	$-i$	$i\bar{\Omega}$	$-i\Omega$	
Γ_{11}	1	-1	-1	i	$-i$	i	-1	1	1	$-i$	i	$-i$	
Γ_{12}	1	-1	-1	$-i$	i	$-i$	-1	1	1	i	$-i$	i	

(b) single-group and double-group irreducible representations of the Wannier orbital basis

state	single group IR	double group IR
$\lvert d_{3z^2-r^2}, \uparrow \rangle$	A'	Γ_7
$\lvert d_{x^2-y^2} - id_{2xy}, \uparrow \rangle$	E'	Γ_{10}
$\lvert d_{x^2-y^2} + id_{2ixy}, \uparrow \rangle$	$\bar{E}'$	Γ_{11}
$\lvert d_{xz-iyz}, \uparrow \rangle$	E''	Γ_8
$\lvert d_{xz+iyz}, \uparrow \rangle$	$\bar{E}''$	Γ_{12}
$\lvert d_{3z^2-r^2}, \downarrow \rangle$	A'	Γ_8
$\lvert d_{x^2-y^2} - id_{2xy}, \downarrow \rangle$	E'	Γ_{12}
$\lvert d_{x^2-y^2} + id_{2xy}, \downarrow \rangle$	$\bar{E}'$	Γ_9
$\lvert d_{xz-iyz}, \downarrow \rangle$	E''	Γ_{11}
$\lvert d_{xz+iyz}, \downarrow \rangle$	$\bar{E}''$	Γ_7

(c) Selection rules for electric dipole transitions, for circular polarization

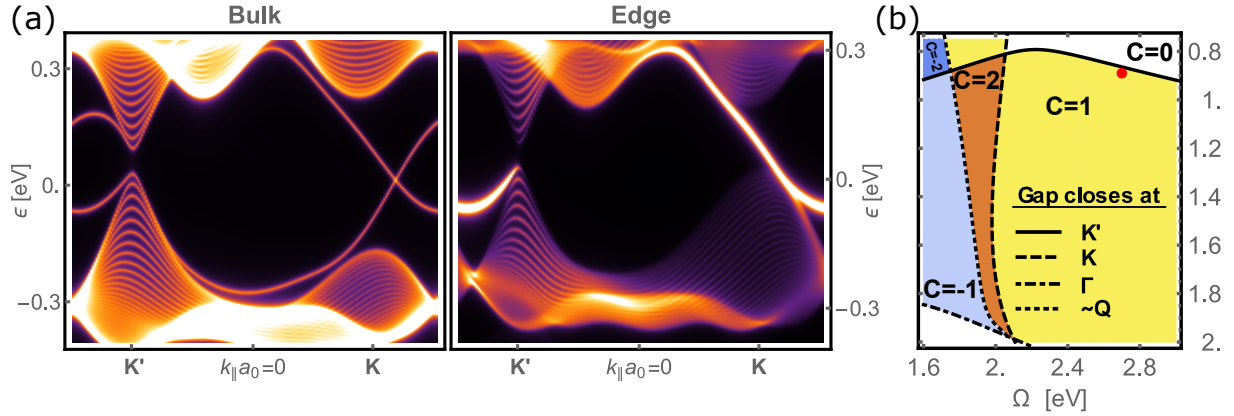| $\bar{C}_{3h}$ IR		$\Uparrow$			$\Downarrow$		
		Γ_7	Γ_{10}	Γ_{11}	Γ_8	Γ_{12}	Γ_9
$\Uparrow$	Γ_7		↻	↻			
	Γ_{10}	↺		↻			
	Γ_{11}	↺	↺				
$\Downarrow$	Γ_8					↻	↻
	Γ_{12}				↺		↻
	Γ_9				↺	↺	

30

Figure S2: Photo-induced inversion of the equilibrium band gap in WS_2 for strong pump fields, for spin-↓. (a) A sufficiently blue-detuned pump field closes the gap selectively at a single valley $\mathbf{K'}$, transitioning into a $\mathcal{C} = 1$ phase. One of the two trivial equilibrium edge states disappears, leaving a single chiral edge mode that spans the band gap. The corresponding phase diagram of Floquet Chern numbers at strong pump strengths is depicted in (b), with (a) corresponding to parameters $A = 0.9, \omega = 2.7eV$. Further increase of the pump amplitude or decrease of frequency triggers additional gap closings at $\mathbf{K}$, $\mathbf{\Gamma}$, and around the second conduction band minimum $\mathbf{Q}$, inducing a mosaic of possible Chern numbers for the photo-modulated valence band. Closing the gap at $\mathbf{K}$, $\mathbf{K'}$ changes the Chern number by ± 1, whereas C_3 symmetry dictates closing the gap at $\mathbf{Q}$ must happen at three points in the Brillouin zone, triggering a change of the Chern number by ± 3. Progressive flattening of the valence band dispersion at strong pump fields indicates the onset of Wannier-Stark physics.